Anisotropy-driven dynamics of cellular fronts in directional solidification in thin samples

Silvère Akamatsu and Gabriel Faivre
Groupe de Physique des Solides, CNRS UMR 75-88, Universités Denis Diderot (Paris VII) et Pierre et Marie Curie (Paris VI), Tour 23, 2 place Jussieu, 75251 Paris Cedex 05, France
(Received 24 March 1998)

We present an experimental investigation of the influence of interfacial anisotropy on the cellular growth patterns observed in directional solidification of the CBr_4-8 mol % C_2Cl_6 alloy at pulling velocities less than twice the cellular-threshold velocity. The experiments are performed with single-crystal samples about 8 mm wide and 12 μm thick. In such samples, the solidification dynamics is essentially two dimensional, and the effective anisotropy of the system can be varied by changing the orientation of the (face centered cubic) crystal with respect to the solidification setup, as was previously established by S. Akamatsu, G. Faivre, and T. Ihle [Phys. Rev. E, **51**, 4751 (1995)]. We find that the cellular pattern is unstable at all values of the spacing λ for crystal orientations corresponding to a vanishing effective interfacial anisotropy. For the other crystal orientations, i.e., for a nonvanishing effective interfacial anisotropy, stable cellular patterns are found over a finite-width λ range. The various modes of instability limiting this range are described. In particular, we show that a homogeneous tilt bifurcation exists for some orientations of the ''degenerate'' type (i.e., such that a {110} plane of the crystal is parallel to the growth direction and perpendicular to the sample plane). This bifurcation is not spontaneous, however, but a consequence of the particular symmetry of the effective interfacial anisotropy of the system for this crystal orientation.
[S1063-651X(98)00609-6]

PACS number(s): 64.70.Dv, 81.30.Fb, 05.70.Ln, 68.70.+w

I. INTRODUCTION

The solid-liquid interface of most metallic alloys and a few transparent organic alloys [1] is rough on a molecular scale. The solidification dynamics of these alloys is mostly controlled by the diffusion of the chemical species preferentially rejected into the liquid by the growing crystal. During solidification, the advancing solid-liquid interface, or growth front, is subjected to morphological instabilities on a scale of a few tenths of micrometers, typically. Basically, these instabilities are due to the fact that the growth rate is proportional to the value of the concentration gradient of the solute at the interface [2]. On the other hand, the amplitude of the deformation of the interface is limited by the capillary effects. As a result of these two competing effects, the growth front generally assumes a more or less stationary, complicated shape, called a solidification pattern.

Solidification patterns have been an object of fundamental research since the late 1940s [3]. One of the main questions of interest has been, and still is, that of the part played by the anisotropy of the interfacial properties in the formation of the patterns. The interfacial properties coming into play are the surface tension γ and the kinetic coefficient β [4]. Since a crystal is an anisotropic medium, γ and β are also anisotropic, i.e., depend on the orientation of the interface with respect to the crystal lattice. In alloys whose solid-liquid interfaces are rough, this anisotropy is weak. For most of these alloys, it remains unknown. It was therefore a surprise when, during the 1980s, several groups of theoreticians came to the conclusion that, although small, the anisotropy of γ (or that of β) plays a major part in the formation of the most commonly observed type of solidification pattern, namely, the dendritic patterns [5]. In laboratory experiments, dendritic patterns are encountered either in free growth or in directional solidification at high values of the growth velocity V (i.e., at $V \gg V_c$, where V_c is the cellular threshold velocity; for definitions of free growth, directional solidification and V_c, see below). It was shown, for two-dimensional (2D) systems, that the very existence of the dendrites relies on the presence of a sufficiently strong interfacial anisotropy. The correlative question of the nature of the necessarily nondendritic patterns that are exhibited by systems of very small interfacial anisotropy in the above experimental conditions (free growth or high-V directional solidification) was also answered recently [6–9].

If the part played by interfacial anisotropy may be considered as essentially elucidated in the case of the (2D) dendritic patterns, it remains largely unclear in the case of the so-called cellular patterns, which are observed in directional solidification at V only slightly larger than V_c. It is indeed a well-known fact that cellular patterns are tilted (the cells have an asymmetric shape and drift laterally along the front) when the crystal is not axially oriented (an axially oriented crystal is a crystal, a symmetry axis of which is parallel to the growth direction), which can only be attributed to interfacial anisotropy [10,11]. It has also been theoretically known for some time that cellular patterns are subjected to symmetry breaking instabilities [12,13], as all modulated fronts are [14]. Experimental reports on such instabilities have been published [15–19]. However, these reports remain elusive on the question of the influence of interfacial anisotropy, mostly for lack of a precise control of the crystal orientation.

In this paper, we present an experimental investigation of the cellular patterns in the alloy CBr_4-8 mol % C_2Cl_6 directionally solidified in thin samples at growth velocities smaller than $2V_c$. In a previous paper [9], called Part I thereafter, the solidification patterns of the same system at higher

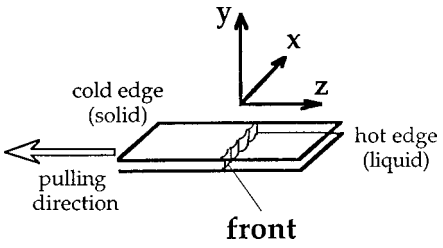

FIG. 1. Definition of the reference frame used in the text.

velocities ($V/V_c > 5$) were investigated. The main specificity of our experiments is that we use very thin single-crystal samples. In such samples, the orientation of the crystal with respect to the solidification setup (in short, crystal orientation) determines the effective interfacial anisotropy of the sample. We are therefore able to bring to light experimentally the dependence of the patterns on the interfacial anisotropy. In the remainder of this Introduction, we shall describe the main ingredients of our experimental method, sum up the previously obtained results concerning the high-V patterns, and, finally, survey the main questions treated in the present study.

CBr_4-C_2Cl_6 is one of the few known transparent organic alloys whose solidification is essentially diffusion controlled. At a concentration of 8 mol % C_2Cl_6, it solidifies into the same phase as pure CBr_4, i.e., a face centered cubic, plastic, crystal phase. The average value of γ in the alloy CBr_4-C_2Cl_6 was measured by several authors [20,21], but, until recently, nothing was known about β_0 and the orientation dependence of γ and β. A systematic comparison between experimentally observed and numerically calculated dendrites in CBr_4-C_2Cl_6 alloys was performed recently in order to determine these unknown quantities. According to that study, kinetic anisotropy is the dominant factor in CBr_4-based alloys [22].

In directional solidification, the sample is placed in an externally applied unidirectional thermal gradient G, and pulled at an imposed velocity V toward the cold side of the gradient. On average, the growth front is parallel to the xy plane and advances with respect to the liquid at the velocity V in the z direction (Fig. 1). At sufficiently low V, the growth front remains planar. Above a finite velocity V_c, which depends on G, it assumes a more or less periodic pattern. This morphological transition is called the cellular, or Mullins-Sekerka, bifurcation [2]. Characteristic features of modulated patterns are the spacing λ, the amplitude A, and the tip radius ρ of the repeat unit. In directional solidification, A increases, and ρ decreases as V increases, while λ shows no simple dependence on V (in fact, λ is not a single-valued function of V, as will be seen below). On this basis, two velocity ranges are usually defined, namely, the cellular, and the dendritic velocity ranges (Fig. 2). Dendrites are characterized by a pointed, parabolic tip and side branches. Cells are usually defined in contrast with the dendrites by their rounded tip ($\rho/\lambda \approx 1$), and absence of sidebranches. The nature of the transition separating the cellular from the dendritic velocity range remains an open question [18,23], which is not addressed in this paper. The velocity range considered in this study ($1.3V_c - 2V_c$) is clearly included in the cellular velocity range. On the other hand, it corresponds to fully nonlinear cellular regimes. (When the cellular bifurcation is supercritical—which is the case in CBr_4-C_2Cl_6 alloys—there exists a weakly nonlinear range immediately above V_c. In our system, this range corresponds to values of $V/V_c - 1$ of the order of 10^{-2} [24], and is not observable experimentally.)

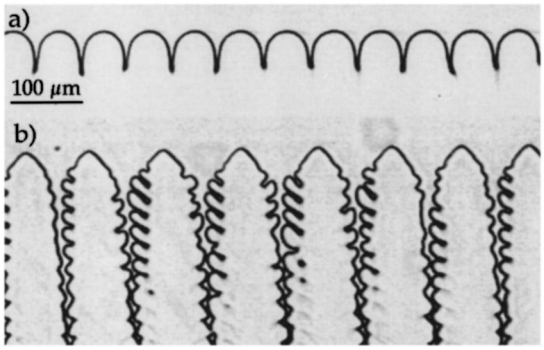

FIG. 2. Optical micrographs of the growth front of an axially oriented crystal of the alloy CBr_4-8 mol % C_2Cl_6 at two different pulling velocities: (a) $V = 4.4\ \mu m\ s^{-1}$. Symmetric-cell pattern; (b) $V = 31\ \mu m\ s^{-1}$. Symmetric-dendrite pattern. $G = 110\ K\ cm^{-1}$. $V_c \approx 2.2\ \mu m\ s^{-1}$. In these images as in the following ones, the growth direction is upward.

The relation between crystal orientation and effective interfacial anisotropy can be treated in the following simplified way. For convenience (but this is not crucial), we suppose that a crystal plane (hkl) and a crystal axis $[uvw]$ are parallel to the sample plane xz and the growth direction z, respectively. We denote the corresponding crystal orientation as $(hkl)[uvw]$. Note that the vector $[uvw]$ is necessarily parallel to the (hkl) plane ($hu + kv + lw = 0$). We also suppose that the interfacial anisotropy is of a purely kinetic origin, and is thus described by the function of two variables $\beta(\mathbf{n})$, where $\mathbf{n}$ stands for the coordinates of the unit vector normal to the interface in the reference frame of the crystal. The following two assumptions are much more crucial (they were validated in Part I; see below).

(1) The solidification dynamics in our very thin samples is entirely 2D, so that $\mathbf{n}$ remains perpendicular to y—i.e., parallel to (hkl)—whatever the deformation of the interface in the xz plane is. Then the dynamics is only sensitive to the one-variable function $\beta(\theta)$, where θ is the angle between $\mathbf{n}$ and z—i.e., $[uvw]$. The function $\beta(\theta)$ is what we call the effective anisotropy of the system for the crystal orientation $(hkl)[uvw]$. Obviously, $\beta(\theta)$ is different for different crystal orientations;

(2) $\beta(\mathbf{n})$ can be approximated as

$$\beta(\mathbf{n}) = \beta_0[1 - \varepsilon_k f_4(\mathbf{n})], \tag{1}$$

where $f_4(\mathbf{n}) = 4(n_1^4 + n_2^4 + n_3^4) - 3$, and $\varepsilon_k \ll 1$. This formula is the expansion of $\beta(\mathbf{n})$ in a power series of the symmetry-invariant combinations of the coordinates of $\mathbf{n}$, truncated after to the first two terms [25]. According to Eq. (1), in the $\{001\}$ planes, $\beta(\theta) \equiv [1 - \varepsilon_k \cos 4(\theta - \alpha_0)]$, where α_0 is the angle between z and a $\langle 100 \rangle$ axis. In the $\{111\}$ planes, $\beta(\theta)$ is a constant. So, to this approximation, the effective anisotropy of our system is at its strongest for the $\{001\}\langle uv0 \rangle$ orientations, and vanishes for the $\{111\}\langle uvw \rangle$ orientations.

Let us now turn to the properties of the dendritic patterns. Let us begin by recalling the previously existing results that motivated the study presented in Part I. In free growth, i.e., growth at given, uniform, undercooling ΔT of the liquid, dendrites grow at a constant rate V and tip radius ρ in the directions corresponding to the maxima of γ or (in our case) the minima of β. The selected values of V and ρ depend on ΔT and the anisotropy coefficient [5,26–28]. [In the case of cubic crystals, free-growth dendrites generally run along the $\langle 100 \rangle$ axes, which is the primary justification of the assumption made in Eq. (1).] In directional solidification, where dendrites grow in an applied thermal gradient and are subjected to substantial near-neighbor interactions, the selection rules involve V, G, and λ [29–31]. Dendrites disappear below a finite value of the anisotropy coefficient, which depends on ΔT—or V in directional solidification [6,7]. Beyond this threshold, dendrites are replaced by pairs of tightly bound symmetry-broken fingers, called split dendrites, or doublons. Contrary to dendrites, doublons are not selected in orientation. They do not form stationary arrays (except under special boundary conditions), but unsteady patterns, called seaweed patterns (the terms of doublon and seaweed pattern were coined by Ihle and Müller-Krumbhaar [7]).

It follows from these theoretical results and the above assumptions that, in the dendritic velocity range of our system, one should observe seaweed patterns for crystal orientations sufficiently close to a $\{111\}\langle uvw \rangle$ orientation (the value of $\langle uvw \rangle$ should not matter much), and dendritic patterns for most other crystal orientations. This is precisely what the experimental observations reported in Part I have shown. For $V \gg V_c$, seaweed patterns are observed when the crystal orientation is within a few degrees of a $\{111\}\langle uvw \rangle$ orientation, while dendritic patterns are observed in all the other cases (with the exception of the $\{001\}\langle 110 \rangle$ orientations, as will be explained shortly). For most orientations, the dendritic patterns are tilted. The relation between the tilt angle α of the dendrites and the control parameters is surprisingly simple: at a given crystal orientation, α is a function of the sole variable $\lambda V/D$, where D is the diffusion coefficient of the solute in the liquid [31]. When the crystal is near a $\{001\}\langle 110 \rangle$ orientation, a peculiar dynamical behavior is observed. In such a ''degenerate'' orientation, two $\langle 100 \rangle$ axes are symmetrically placed about z, corresponding to two possible dendritic patterns tilted at $+45°$ or $-45°$. It was found that these dendritic patterns are stable (domains of the two different dendritic patterns are formed) at V/V_c larger than about 8, and unstable at lower values of V/V_c. In the range $5 < V/V_c < 8$, an unsteady pattern, called ''degenerate,'' sets in.

We can now turn to the subject of the present study, and briefly survey the main topics to be considered below. The first question, suggested by the results of Part I, is whether, or not, interfacial anisotropy is a necessary condition for the existence of stationary cellular patterns. Our results can be summed up as follows. For most crystal orientations, we observed stable cellular patterns over finite ranges of λ. But for the orientations that give rise to seaweed patterns at high V, i.e., the orientations close to $(111)\langle uvw \rangle$, we never observed stable cellular patterns, but only unsteady patterns of the type illustrated in Fig. 3. It is thus natural to conclude that the width of the λ-stability range of the cellular patterns is finite if, and only if, the interfacial anisotropy is sufficiently strong. This conclusion is similar to the one recently reached by Kopczynski, Rappel, and Karma in their numerical stability analysis of the cellular patterns in a symmetrical system (i.e., a system with the same diffusion coefficient in the solid and the liquid) [32].

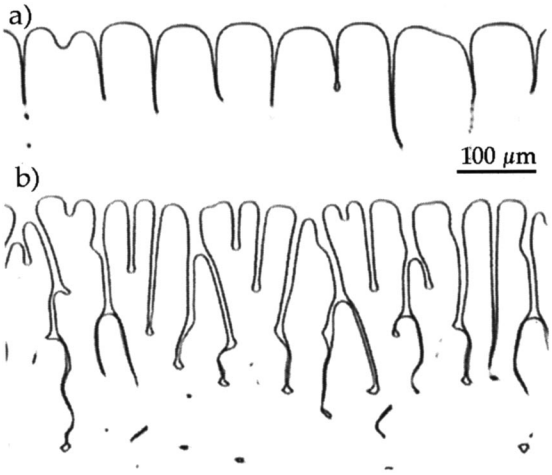

FIG. 3. Growth front of a nearly $\{111\}\langle uvw \rangle$-oriented crystal at two different pulling velocities: (a) $V = 3.1\ \mu\text{m s}^{-1}$. Unsteady cellular pattern; (b) $V = 31.1\ \mu\text{m s}^{-1}$. ''Seaweed'' pattern.

Another question studied below is that of the origin of the tilt of the cellular patterns. For most nonaxial crystal orientations—for instance, in the case illustrated in Fig. 4—the cellular patterns are tilted, and their tilt angle smoothly increases with increasing λ at given V. In the case of degenerate orientations, a different behavior is observed. We show below that patterns consisting of an alternation of domains of symmetric, and tilted cells are observed for at least some of the orientations belonging to the degenerate-orientation family. Since it is known from the study of other types of modulated fronts that such patterns are the sign of an underlying tilt bifurcation of the system as a function of λ at given V, we conclude that such a bifurcation exists also in our system for the degenerate orientations. The question, raised by some authors [15,16], of whether the tilt of the cellular patterns is due to an underlying ''spontaneous'' bifurcation must thus

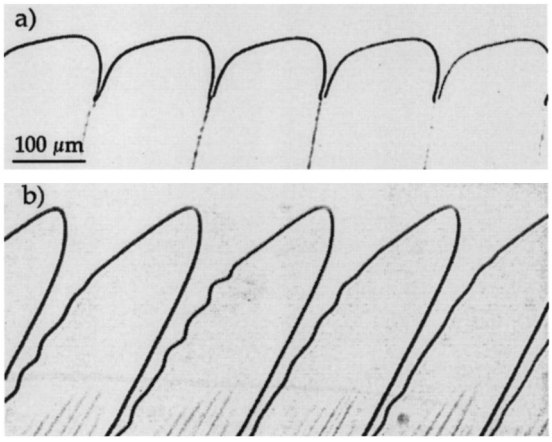

FIG. 4. Growth front of a nonaxially-oriented crystal at two different pulling velocities: (a) $V = 3.1\ \mu\text{m s}^{-1}$. Tilted-cell pattern; (b) $V = 31.1\ \mu\text{m s}^{-1}$. Tilted-dendrite pattern.

TABLE I. Some physical constants of the alloy CBr_4-C_2Cl_6. T_m: melting temperature of pure CBr_4. m: liquidus slope (absolute value). K: partition coefficient. D: diffusion coefficient of the solute in the liquid. γ: solid-liquid surface tension. L: latent heat of melting. The uncertainties are of the order of 1% on T_m and L, and 10% on the other quantities [21].

T_m (°C)	m (K mol^{-1})	K	D (m^2 s^{-1})	γ (mJ m^{-2})	L (kJ mol^{-1})
92.5	80	0.75	5×10^{-10}	6.6	3.35

be answered in the following way: in the cellular patterns, the tilt is always due to the interfacial anisotropy, even when it takes on the form of a homogeneous tilt bifurcation (a spontaneous tilt bifurcation cannot be observed because no stability range of the symmetric or tilted cellular patterns exists in the absence of interfacial anisotropy). This conclusion is supported by numerical calculations recently performed by Ihle (unpublished results).

The preceding questions are but particular aspects of the vaster question of the modes of instability of the cellular patterns as a function of the interfacial anisotropy. A systematic experimental study of this question would mean a complete exploration of the space (λ, V, G) for each orientation (see, for instance, [18,19]). We have not attempted to perform such a systematic investigation, but contented ourselves with studying five representative crystal orientations at a given value of V/V_c. The types of instabilities that we have encountered are the cell termination, the cell splitting, the T-$1\lambda O$ and the $2\lambda O$ instabilities. (In modulated fronts, the oscillatory modes of instability are usually denoted by a symbol $x\lambda O$, where $x\lambda$ stands for the space period of the oscillation. The modes in which a tilting of the pattern is combined with an oscillation are denoted T-$x\lambda O$. For instance, the symbol $2\lambda O$ denotes a period-doubling oscillatory mode, and the symbol T-$1\lambda O$ a tilted, period-preserving oscillatory mode—see, for instance, [33] and references therein.) The conditions of occurrence of these instabilities are strongly orientation dependent. As a general trend, it can be stated that a strong interfacial anisotropy stabilizes the cellular patterns against all the types of instability.

II. EXPERIMENTAL METHODS

Some physical constants of the CBr_4-C_2Cl_6 system are given in Table I. The details about the experimental methods can be found elsewhere [9,21,34]. A few facts must be recalled here. The alloy is made by mixing the zone-refined compounds. The samples are made of two parallel glass plates separated by two calibrated poly-(ethylene terephthalate) strips. The free space limited by the glass plates and the strips is about 12 μm thick, 8 mm wide, and 70 mm long. This space is filled with the molten alloy at a relatively high temperature (≈100 °C). A non-negligible amount of gas is dissolved in the melt during this process. During a given solidification run, the average value of V is controlled up to within less than 1%, but the instantaneous value undergoes a slow periodic modulation of amplitude about 4%, due to a slight misalignment of the pulling system. The time period of the modulation is equal to the pitch of the pulling micrometric screw (1 mm) divided by V.

In this study, the applied thermal gradient is $G=110\pm10$ K cm^{-1}. The nominal concentration of the alloy is 8 mol % C_2Cl_6. The effects due to the above-mentioned residual gas (residual-impurity effects) are detectable, but unimportant for our present purpose, as will be seen in Sec. III A. As in Part I, single crystals were grown by means of funnel-shaped spacers. The orientation of the crystal is not known *a priori*. The determination of the crystal orientation by x-ray diffraction after the run is not practicable, mostly because of the solid-solid phase transition of CBr_4 at ≈43 °C. In Part I, the crystal orientation was determined *in situ* independently of the growth patterns by observing the shape of faceted gaseous inclusions in the crystal. For this method to be applied, a relatively large gas bubble must be present in the liquid before the run (it can also be nucleated during the run), and engulfed in the solid during solidification. This is accompanied by perturbations of the pattern, which are rapidly relaxed at high V, but not in the cellular velocity range. Therefore, we did not use the faceted-bubble method in this study. We contented ourselves with deducing the crystal orientation from the characteristics of the high-V growth patterns. For this purpose, prior to the low-V run devoted to the study of the cellular patterns, we carried out a short run at a relatively high velocity $(V/V_c\approx10)$, noted the characteristics of the pattern at that velocity, and then remelted the solid back to its initial position (the initially selected crystal was thus conserved). Thanks to the previously accumulated data, this method proved satisfactory for the present study.

During the experimental runs, the growth front is continuously observed with an optical microscope. The images are transferred to a tape recorder, and digitized for further analysis [35]. In this study, V ranged from 3.1 to 4.5 μm s^{-1}. The total pulling time at a given value of V was usually of a few 1000 s, corresponding to a solidified length of the order of 10 mm. The duration time of the runs was thus always much longer than the diffusion time $\delta=D/V^2$ (≈50 s for $V=3.1$ μm s^{-1}). In some cases, two successive runs at different values of V were applied to the same crystal. Longer runs were not applied in order to avoid the perturbations occurring when the front approaches the hot end of the samples (these perturbations are mostly due to the slow evaporation of CBr_4 and C_2Cl_6 through this end of the sample). A relatively low magnification was used in order to observe a large portion of the growth front. The field was 2500-μm wide, and contained 30 to 50 cells, which represents about one-third of the total width of the sample.

Spatiotemporal (ST) diagrams of the front were performed as follows. At regular time intervals, a line normal to the growth direction is selected at a given distance behind the foremost point of the front, and recorded. When the lines have been stored in sufficient number, they are piled up along an axis representing the time. The ST diagrams essentially show black lines corresponding to the trajectories of the narrow liquid grooves separating the cells (intercellular grooves). The local, instantaneous values of the spacing λ and the tilt angle α (defined by $\tan\alpha=V_d/V$, where V_d is the lateral drift velocity of the repeat unit) are extracted from the ST diagrams. λ is measured as the distance between two

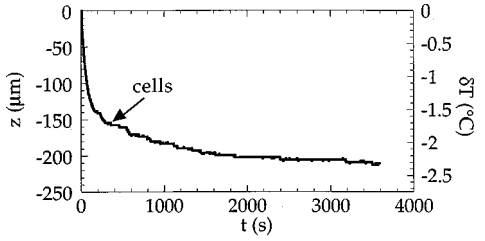

FIG. 5. Position z and undercooling $\delta T(=Gz)$ of the front as a function of time measured during the initial transient (recoil curve) for a sample pulled at $V=3.1\ \mu\mathrm{m\ s^{-1}}$.

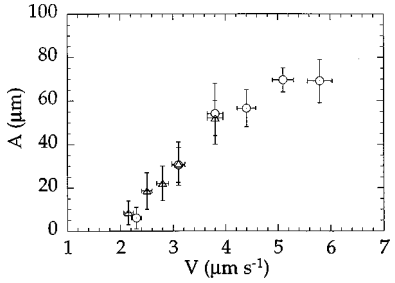

FIG. 6. Amplitude A of the cells in symmetric-cell patterns as a function of V. The circles and the triangles correspond to different samples. The vertical bars represent the dispersion of the A measurements. The horizontal bars correspond to the variation of V during the pulling.

adjacent liquid grooves, with an uncertainty of $\pm 2\ \mu$m. α is measured as the angle between the pulling axis and the trajectories of the liquid grooves, with an uncertainty of the order of $\pm 0.2°$ (including the error due to the periodic modulation of V).

III. PRELIMINARY RESULTS

A. Initial transient. Residual-impurity effects

Before reaching a permanent state, a directionally solidified sample undergoes a transient—called initial, or solute-redistribution, transient—corresponding to the progressive accumulation of the chemical species rejected by the solid in the liquid ahead of the front [36]. The terminal stage of the transient is exponential in time, with a characteristic time depending on the partition coefficient of the species considered. The partition coefficient K of C_2Cl_6 being close to 1, the corresponding transient time is equal to δ. The partition coefficient K_i of the (dominant) residual impurity being much smaller than 1 ($K_i \approx 0.02$) [34], the corresponding transient time is $\delta/K_i \gg \delta$. Consequently, the initial transients in our system can be divided into a first short stage corresponding to the accumulation of C_2Cl_6, and a long-lasting terminal stage during which the residual impurities continue to slowly accumulate. The V jumps are also followed by a two-stage solute-redistribution transient, whose characteristic times are $\delta_{12}=D/V_1V_2$, and δ_{12}/K_i, respectively, where V_1 and V_2 are the values of V before and after the V jump.

Apparently, the slow accumulation of the residual impurities during the terminal stage of the initial transient has no noticeable effect on the dynamics of the front, provided that V is not too close to V_c [37]. In Fig. 5, the recoil curve (i.e., the position of the front as a function of time, the origin being taken at the onset of the pulling) of a sample pulled 1 h at $V/V_c \approx 1.5$ is reproduced. The cellulation began at $t_c \approx 300$ s. For $t > t_c$, the quantity shown in the figure is the position of the cell tips. It can be seen that the cell tips practically cease to recoil after a time (≈ 2000 s) much smaller than $\delta/K_i (\approx 10^4$ s). The observations moreover showed that not only the position, but also the shape of the cells remained essentially stationary after that time. Only near the bottom of the grooves did a slow, complicated, evolution (including, in some cases, the emission of liquid droplets [38]) continue to take place, indicating that the residual impurities are rapidly segregated into the intercellular grooves. The only observed unexplained effect that might be attributed to residual impurities is a slight continuous increase of the tilt angle, which was sometimes observed in the case of tilted patterns.

Quantitative information about the residual impurities can be gained from the recoil curves and the cellular-bifurcation velocity threshold. When the front is planar (i.e., when $V/V_c < 1$), the final recoil of the front is equal to the sum of the thermal lengths $l_{\mathrm{th},\sigma}$ relative to the different solutes of the alloy, defined by $l_{\mathrm{th},\sigma}=\Delta T_{0,\sigma}/G$, where $\Delta T_{0,\sigma}=m_\sigma(K_\sigma^{-1}-1)C_\sigma$ is the thermal gap, m_σ the slope of the liquidus, K_σ the partition coefficient and C_σ the concentration of solute σ (it is assumed that all solutes are in low concentration). In our alloy, the thermal length relative to C_2Cl_6 (thereafter called the nominal thermal length) is $l_{\mathrm{th}}^{\mathrm{nom}} \approx 196\ \mu$m. In the case illustrated in Fig. 5, the final recoil of the cell tips was of $\approx 215\ \mu$m, and the cell amplitude had a value of $\approx 40\ \mu$m. The (theoretical) position of the planar front, obtained by averaging the cellular front over x, is $230 \pm 10\ \mu$m. Knowing K_i and m_i (≈ 50 K) [34], one obtains $C_i = 3\times 10^{-4}$ mol.

B. Cell amplitude. Cellular-threshold velocity

For a single-component alloy, the cellular threshold velocity is given by [2]

$$V_c \simeq \frac{D}{1_{\mathrm{th}}}\left[1+3\left(\frac{d_0K^2}{41_{\mathrm{th}}}\right)^{1/3}\right]+o\left[\left(\frac{d_0}{1_{\mathrm{th}}}\right)^{1/3}\right], \qquad (2)$$

where $d_0=\lambda T_m/(L\Delta T_0)$ is the capillary length, L the latent heat, and T_m the melting temperature of the pure solvent. The nominal value of V_c in our system is thus $V_c^{\mathrm{nom}} \approx 2.8\ \mu\mathrm{m\ s^{-1}}$ (note that this value is about 10% larger than the zeroth-order value $D/l_{\mathrm{th}}^{\mathrm{nom}} \approx 2.55\ \mu\mathrm{m\ s^{-1}}$). In the case of a dilute multi-component alloy, V_c^{-1} is approximately equal to the sum of the reciprocals of the values given by Eq. (1) for each component.

The actual value of V_c in our samples was determined experimentally by measuring the amplitude A of the cells, defined as the distance between the cell tips and the groove bottoms, as a function of V, and extrapolating the data to $A=0$. This was done for four different samples of crystal orientation close to $\{001\}\langle 100\rangle$. Figure 6 shows the values of $A(V)$ obtained through a series of downward velocity jumps in two different samples. After each V jump, we waited during a period of a few δ_{12} before performing the measurements. We verified that a steady state had been reached in the

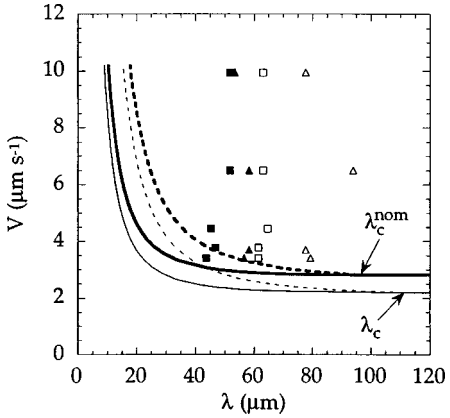

FIG. 7. Symbols: measured values of the intercell spacing λ. Squares: axially oriented sample. Triangles: non-axially-oriented sample. The filled and open symbols correspond to the lower and upper observed values at a given V, respectively. Curves: calculated marginal-stability (plain line) and most-dangerous-mode (dashed line) curves. The thick-line and thin-line curves correspond to calculations without and with residual impurities ($C_i = 3\times10^{-4}$) being taken into account, respectively.

region of the cell tips by this time. The large error bars in Fig. 6 essentially represent the dispersion of the position of the groove bottoms (the position of the cell tips showed no detectable dispersion). By extrapolating the $A(V)$ data to $A=0$, we found $V_c \approx 2.2 \pm 0.2\ \mu\mathrm{m\ s}^{-1}$ for the four samples studied. The value of C_i that can be calculated from the value of $V_c^{\mathrm{nom}} - V_c$ is $C_i \approx 2\times10^{-4}$, which is consistent with the estimate given in Sec. III A.

C. Intercellular spacing

During the last few years, an increasing number of experimental and theoretical results have indicated that no wavelength selection in the strict sense of the term occurs in solidification fronts [18,23,33,39,40]. For a number of systems, numerical calculations showed that the width of the range of λ at which the pattern is stationary at given V (λ stability range) is finite. Experimentally, it was found that, as a general rule, the spatial λ distributions of solidification fronts are nonuniform from the beginning to the end of the solidification runs. An additional support to this conclusion is given by the observations reported below. In this section, our only purpose is to compare the observed values of λ with the so-called marginal stability and most dangerous values of λ. Let us recall the definition of these notions. The linear stability analysis of the planar front at fixed G leads to the dispersion equation giving the amplification coefficient ω of a sinusoidal perturbation applied to the planar front as a function of the wavelength λ of this perturbation and V. In the plane (λ, V), the equations of the marginal-stability and most-dangerous-mode curves are $\omega(\lambda, V) = 0$ and $\partial\omega/\partial\lambda(\lambda, V) = 0$, respectively. The dispersion equation for a binary alloy can be found elsewhere [2], and is easily extended to the case of a dilute ternary alloy.

Figure 7 shows the marginal-stability and most-dangerous-mode curves calculated for a CBr_4-8 mol % C_2Cl_6 alloy, together with values of λ measured in two different samples over a range of V extending from $V < 2V_c$ to values

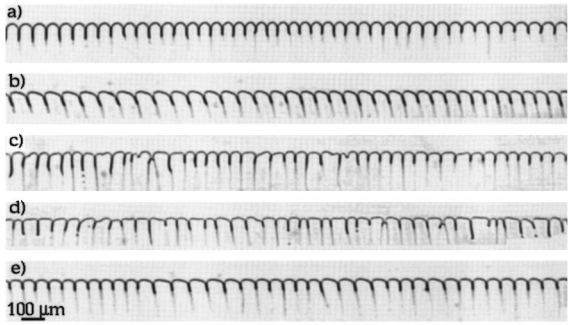

FIG. 8. Cellular fronts observed in five single-crystal samples of different orientations: (a) symmetric-cell pattern in a crystal of nearly axial orientation ($V = 3.4\ \mu\mathrm{m\ s}^{-1}$); (b) tilted-cell pattern in a crystal of high-anisotropy nonaxial orientation ($V = 4.4\ \mu\mathrm{m\ s}^{-1}$); (c) unsteady pattern in a crystal of vanishing-anisotropy orientation ($V = 3.77\ \mu\mathrm{m\ s}^{-1}$); (d) unsteady pattern in a crystal of high-anisotropy degenerate orientation ($V = 3.77\ \mu\mathrm{m\ s}^{-1}$); (e) tilt-domain pattern in a crystal of low-anisotropy degenerate orientation ($V = 3.44\ \mu\mathrm{m\ s}^{-1}$). The snapshots were taken near the end of the runs.

belonging to the dendritic velocity range. In one of the samples, the crystal was axially oriented and the cells were symmetric, while, in the other, the crystal was nonaxially oriented and the cells were tilted. In both samples, a stationary finite-width distribution of λ was observed. In Fig. 7, the minima and maxima of these distributions are plotted. Several facts are noteworthy. The extremum values of λ do not vary significantly with V, even in the transition range from cells to dendrites. The values of λ are significantly higher in the tilted than in the symmetric pattern (we shall return to this below). For the symmetric pattern, the observed values

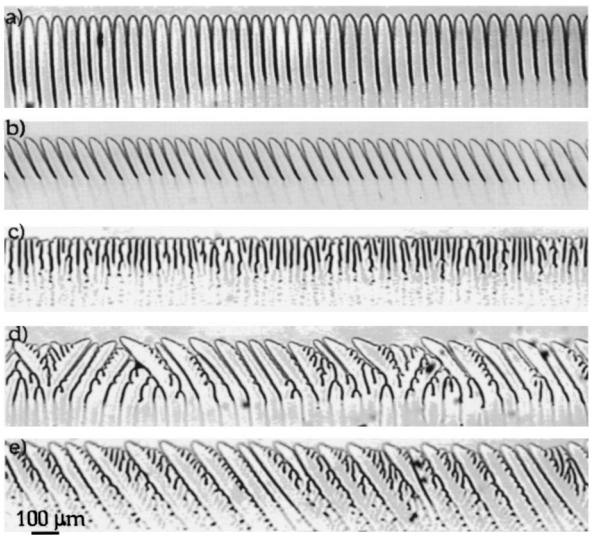

FIG. 9. High-V patterns of the same crystals as in Fig. 8: (a) symmetric dendrites ($V = 31.1\ \mu\mathrm{m\ s}^{-1}$); (b) tilted dendrites ($V = 23.9\ \mu\mathrm{m\ s}^{-1}$); (c) seaweed pattern ($V = 31.1\ \mu\mathrm{m\ s}^{-1}$); (d) coexistence of rightward- and leftward-tilted dendrites ($V = 31\ \mu\mathrm{m\ s}^{-1}$; the leftward-tilted dendrites prevailed after a long time of pulling); (e) tilted low-anisotropy dendrites ($V = 31.1\ \mu\mathrm{m\ s}^{-1}$). In (a) and (b), the absence of detectable sidebranches at these values of V/V_c and λ is due to the predominance of kinetics effects in the alloy CBr_4-C_2Cl_6.

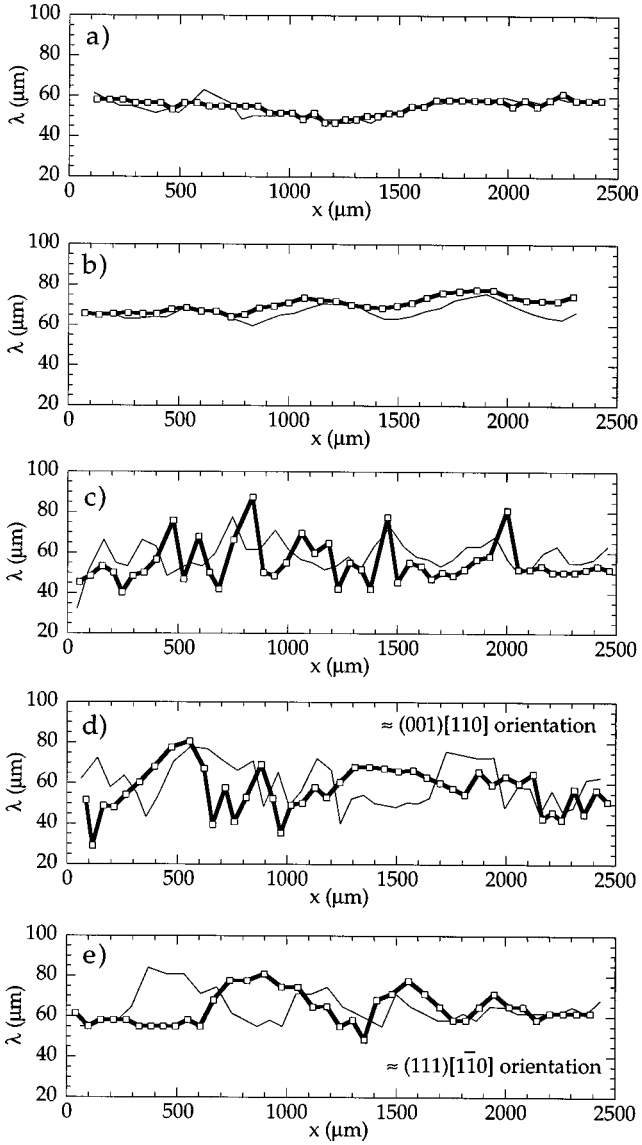

FIG. 10. Plots of the intercell spacing λ as a function of the position x along the front (λ plots) for the same crystals as in Fig. 8. The thick-line curves correspond to the snapshots shown in that figure, i.e., to the end of the runs. The thin lines curves were measured at substantially earlier times.

of λ near threshold are noticeably smaller than the critical wavelength at threshold, and comparable with the most dangerous wavelength, in agreement with theoretical predictions [24,32]. Since, roughly speaking, the average spacing λ is independent of V, λ/l_d is proportional to V^{-1}. Near threshold, it has a value of about 0.5.

IV. THE CELLULAR PATTERN AS A FUNCTION OF THE CRYSTAL ORIENTATION

A. Overview

We shall now proceed to a description of five illustrative experimental runs, which were performed at velocities smaller than $2V_c$ with five single crystals of different orientations. We shall designate the crystals by the labels *a* to *e*. Snapshots of the five cellular patterns near the end of the runs are shown in Figure 8. Snapshots of the high-V patterns

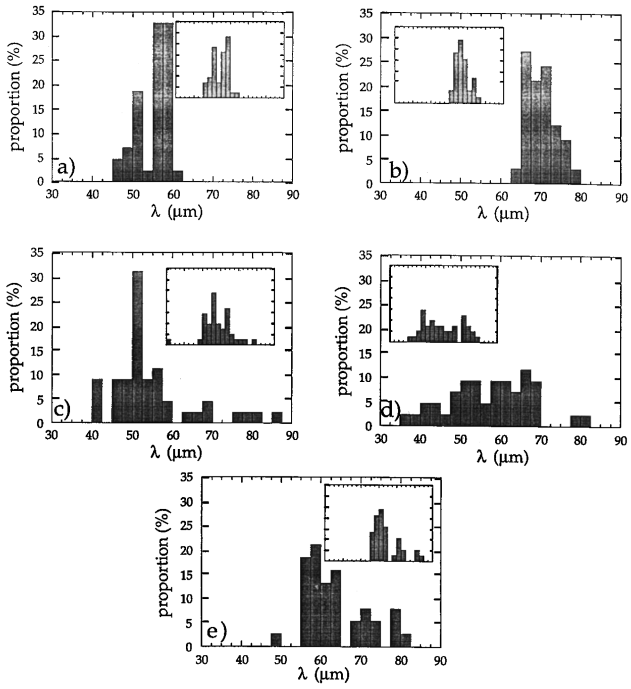

FIG. 11. Histograms of the intercell spacing for the same crystals as in Fig. 8. The full-scale figures correspond to the thick-line plots in Fig. 10, and the insets to the thin-line ones.

are shown in Fig. 9. Spatial distributions of λ (λ plots) and λ histograms are given in Figs. 10 and 11, respectively, for the five runs. The entire spatiotemporal diagrams of the runs (excluding the initial transient) are given separately in Figs. 12–16. The orientations of crystals *a* to *e* will now be discussed, and the main specific features of their respective cellular patterns pointed out. The full spatiotemporal diagrams will be analyzed one after the other in the following sections.

1. Crystal a

The symmetrical dendrites appearing in Fig. 9(a) indicate that the crystal was close to a (001)[100] orientation. Generally speaking, a distinction must be made between in-plane and off-plane misorientations with respect to the ideal (001)[100] orientation, corresponding to rotations about [001] (the in-plane angle of rotation is α_0), and an axis perpendicular to [001], respectively. The amplitude of the effective anisotropy is unaffected by an in-plane misorientation,

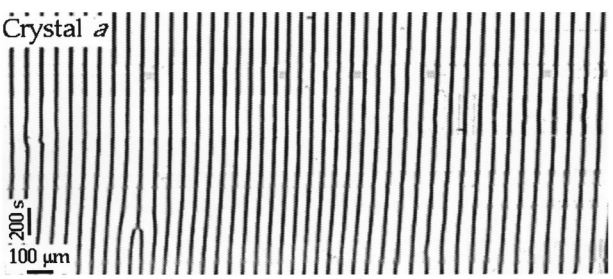

FIG. 12. ST diagram of the symmetric-cell pattern shown in Fig. 8(a). In this ST diagram as in the following ones, time is running upward; in terms of lengths, the vertical scale is much smaller than the horizontal one, so that the apparent tilt angle is much larger than the real one.

but decreases with an increasing off-plane misorientation. In the case of crystal *a*, both types of misorientations are small. In Figs. 8(a) and 10(a), it can be seen that, up to a negligible tilt ($\approx 0.7°$), the cellular pattern of crystal *a* is reflection symmetric and stationary in the laboratory reference frame. An enlarged view of a similar pattern observed in another (001)[100]-oriented crystal is given in Fig. 1(a). Moreover, the λ plot is smooth [Fig. 10(a)] and the λ histogram is narrow [Fig. 11(a)]. The average value of the spacing is $\lambda \approx 55\ \mu$m. The half-width of the histogram is about 10% of λ.

2. Crystal b

The tilted dendrites appearing in Fig. 9(b) ($\alpha \approx 32°$) indicate that the crystal had a large in-plane misorientation with respect to the (001)[100] orientation, and a negligible off-plane misorientation. The value of α_0 calculated with the help of the previously established similarity law [31] is $37 \pm 4°$. As in the case of crystal *a*, the cellular pattern of crystal *b* has a smooth λ plot [Fig. 10(b)] and a narrow λ histogram [Fig. 11(b)]. However, the cells now have an asymmetric shape and drift laterally in the same direction as the high-*V* dendrites [Fig 8(b); another example is given in Fig. 4]. The average values of the tilt angle and the spacing are $\alpha \approx 5°$ and $\lambda \approx 70\ \mu$m, respectively. Note that λ is significantly larger than in crystal *a*.

3. Crystal c

The high-*V* pattern of this crystal [Fig. 9(c)] is of the seaweed type. (This was most clearly revealed by the ST diagram at high *V*, not shown). The crystal orientation was thus close to $(111)[uvw]$. The cellular pattern is strikingly irregular and unsteady [Figs. 8(c) and 10(c)]. An enlarged view of a similar pattern observed in another crystal is given in Fig. 3. The λ histogram [Fig. 11(c)] exhibits long tails. These tails indicate that a population of unsteady cells (cells that are being destroyed by tip splitting or terminated by pinching off) is permanently present.

4. Crystal d

The high-*V* patterns of this crystal [Fig. 9(d)] is of the degenerate type. An in-plane misorientation of a few degrees relative to the ideal (001)[110] orientation is sufficient to eliminate the characteristic features of the degenerate dynamics (see Part I). So does also an off-plane misorientation corresponding to a rotation about the [110] axis. On the other hand, an off-plane misorientation corresponding to a rotation about the [110] axis does not destroy the degenerate nature of the effective anisotropy, but simply makes its amplitude smaller. In the case of crystal *d*, all types of misorientation were small. A slight preference for the leftward tilt direction was, however, noted. The cellular pattern [Fig. 8(d)] exhibits wide domains of regularly spaced tilted cells (tilt domains) separated by narrow disordered regions.

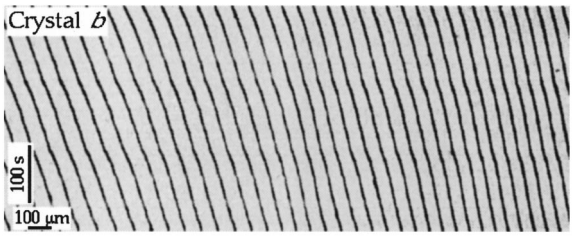

FIG. 13. ST diagram of the tilted-cell pattern shown in Fig. 8(b).

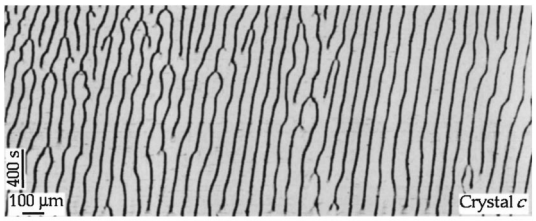

FIG. 14. ST diagram of the unsteady pattern shown in Fig. 8(c).

5. Crystal e

The high-*V* pattern of this crystal [Fig. 9(e)] shows dendrites tilted to an angle of about 45°. A detailed inspection of the high-*V* dynamics (not reproduced here) showed that the orientation of the crystal was degenerate with a large misorientation about the [110] axis. In particular, a seaweed pattern was transitorily observed at $V = 31\ \mu\text{m s}^{-1}$, indicating that the anisotropy level was very low. A small, but noticeable, in-plane misorientation to the left of the figure was also present. The cellular pattern of crystal *e* clearly exhibits a structure in domains of alternately tilted and symmetric cells [Figs. 8(e) and 10(e)]. The coexistence of two populations of cells can also be deduced from the appearance of two maximums in the λ histogram in Fig. 11(e).

B. The high-anisotropy axial orientation (crystal *a*)

1. Nonuniform stationary λ distributions

The main characteristic feature of the solidification dynamics of our system for the (nondegenerate) high-anisotropy crystal orientations is the existence of nonuniform, stationary λ distributions. This implies that the phase-diffusion mechanism, which tends to smooth out small-amplitude, large-wavelength modulations of λ, is ineffective. In order to substantiate this conclusion, let us examine the ST diagram of crystal *a* (Fig. 12). The onset of the cellulation occurred during the initial transient, and was rapidly followed by the elimination of a large number of cells. Since it provokes a strong increase of λ, this process slows down rapidly, and ends with a last, isolated, cell-termination event. This final event is included in the ST diagram shown in Fig. 12. It can be seen in Fig. 10(a) (at $x \approx 650\ \mu$m) that the cell-termination event leaves behind a bump in the λ plot,

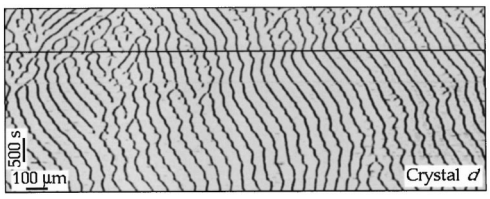

FIG. 15. ST diagram of the unsteady pattern shown in Fig. 8(d). The horizontal line signals a downward velocity jump from 3.7 to $3.5\ \mu\text{m s}^{-1}$.

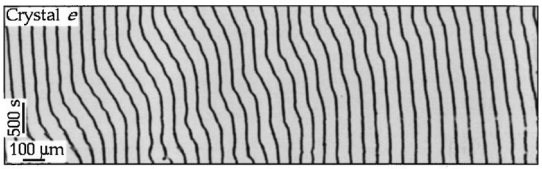

FIG. 16. ST diagram of the pattern shown in Fig. 8(e).

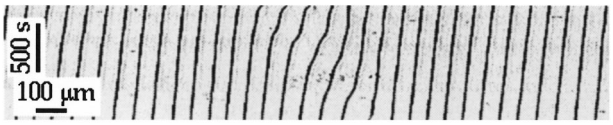

FIG. 17. ST diagram of a cellular pattern observed in a crystal of high-anisotropy, slightly nonaxial orientation, showing a solitary wave.

which smooths out relatively rapidly, but not completely. Afterwards, the λ distribution, although still nonuniform, does not evolve any more. Without entering into more details, the following conclusion of general validity can be drawn: the final λ distribution is the result of the numerous, only partly relaxed, cell-termination events occurring during the initial transient. The details of this distribution depend on the whole sequence of cell-termination events, which is itself determined by the complicated spatiotemporal correlation existing between the events. This accounts for the apparent unpredictability of the details of the λ distribution. On the other hand, its global characteristics (smoothness, small amplitude) do not depend on these details. In the case of crystal *a*, the relative amplitude of the λ modulation is ± 0.1, and the characteristic wavelength is about 20 cells. Note that regions containing 5 to 10 cells, in which λ is practically uniform, can be found. The same characteristics were observed in all the crystals of non-degenerate high-anisotropy orientation that we studied.

2. Cell-termination instability

The cell-termination events are of common occurrence in most modulated patterns. It is tempting to interpret them as the result of an Eckhaus instability. This instability, we recall, corresponds to the fact that the phase-diffusion coefficient of the pattern goes to zero at a certain value of λ, and is negative beyond this value. A negative phase-diffusion coefficient means a spontaneous amplification of the spatial λ modulations, which is likely to lead to the elimination of a cell. This explanation of the cell-termination event is, however, not satisfactory in the case of solidification fronts. It seems difficult to reconcile it with the fact that phase diffusion is apparently ineffective at spacings only slightly larger than that at which the cell-termination events occur. Unfortunately, this point is difficult to clarify experimentally because the displacements involved are very small. A few remarks can, however, be made. In Figs. 8(a) and 10(a), it can be seen that the initial width of the eliminated cell was indeed small (40 μm), but this cell was not surrounded by a wide trough of the λ distribution, as it would in a phase-diffusion controlled process. The smoothing out of the bump in the λ distribution subsequent to the event is first rapid, and then stops suddenly, which is again at least unusual for a diffusive process. In fact, a close inspection of the λ plots at short times intervals (not reproduced here) reveals that the elimination of the cell is accompanied with a slight, damped oscillation of short wavelength (the oscillations of near-neighbor cells are out of phase). A similar observation was recently made in the cellular patterns of a succinonitrile (SCN)-based alloy [18]. In lamellar eutectic fronts, the following mechanism is observed [41]: in addition to the oscillation, two small, evanescent, tilt waves are emitted, which carry away the excess of spacing over a distance of a few λ, and then disappear. This type of process is undoubtedly conceivable here also (other examples of interplay between the oscillatory and the tilt modes of instability are given below).

3. Stability domain of the symmetric cellular pattern

The above observations show that the symmetric cellular pattern has a wide stability range in the case of high-anisotropy axial crystal orientations. The lower bound λ_- of the stable range corresponds to the cell-termination instability. In the above example (crystal *a* at $V=3.4\ \mu\mathrm{m\ s^{-1}}$), a large plateau at $\lambda=47\ \mu$m was apparently stable, whereas cells of spacing smaller than 40 μm were eliminated. We therefore conclude that $40\ \mu\mathrm{m}<\lambda_-<47\ \mu\mathrm{m}$. In an attempt to determine the velocity dependence of λ_-, four successive upward velocity jumps were applied to crystal *a* (the successive values of *V* were 3.4, 3.8, 4.4, 6.5, and 9.9 $\mu\mathrm{m\ s^{-1}}$). A single additional cell-termination event took place after the *V* jump from 4.4 to 6.5 $\mu\mathrm{m\ s^{-1}}$, for $\lambda\approx 44\ \mu$m. This suggests (but does not prove because of the experimental uncertainties connected with the post-jump transients) that λ_- increases slightly with increasing *V* in our system.

Little can be said about the upper bound λ_+ of the stability range of the symmetric cellular pattern. In the case of crystal *a*, we did not observe any instability on the large λ side at the initial pulling velocity of 3.4 $\mu\mathrm{m\ s^{-1}}$, which is not surprising since the final λ distribution was reached from low values of λ. More surprisingly, we practically never succeeded in triggering large-λ instabilities in (001)[100]-oriented crystals, whatever pulling history we tried. The only exception was the solitary tilt wave shown in Fig. 17 (for the distinction between solitary tilt waves and tilt domains, see [33]). We can therefore only state that λ_+ is substantially above the highest observed value of λ ($\approx 61\ \mu$m), at all velocities.

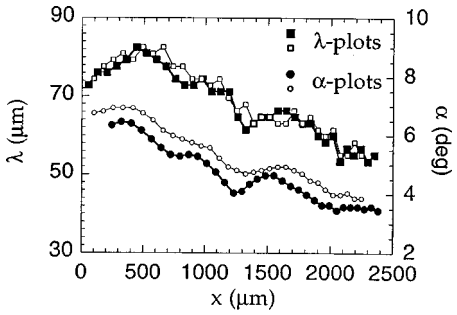

FIG. 18. Spacing- and tilt-angle-plots in crystal *b* at two different times, extracted from Fig. 13. The filled symbols correspond to an earlier time than the open ones (time interval ≈250 s).

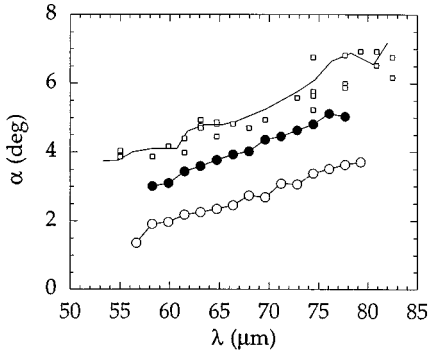

FIG. 19. Tilt angle as a function of spacing in crystal *b*. Squares: data extracted from Fig. 18. The curve running through the data is a time average of the measurements. Circles: data from another sample at $V=3.4\ \mu\mathrm{m\ s^{-1}}$ (open circles) and $V=3.7\ \mu\mathrm{m\ s^{-1}}$ (filled circles).

C. The high-anisotropy nonaxial orientation (crystal *b*)

The most interesting feature to be noted in the ST diagram of crystal *b* (Fig. 13) is that α, like λ, is nonuniformly distributed along the front. Consider first the λ distribution. It can be analyzed as the superposition of a gradual increase of λ (from 60 to 80 μm) from the right-hand to the left-hand side of the front, and a small-amplitude modulation. As above, the small-amplitude modulation stems from the series of cell-termination events occurring immediately after the onset of the cellulation. The origin of the long-range λ gradient is as follows. The very existence of an extended tilted pattern obviously implies that new cells are continually emitted by a source located at the edge of the sample opposite to the direction of the drift (here, the right-hand edge). The new cells are emitted by the source at a definite spacing (at given *V*), which is generally different from the (average) spacing of the ''old'' cells resulting from the primary cellulation. In the present example, the new cells had a smaller spacing than the old ones, which accounts for the λ gradient observed.

The λ and α plots in crystal *b* at two different times of pulling are plotted in Fig. 18. Except for a slight uniform upward shift of α, whose origin is unclear (it may be due to the slow modulation of the pulling velocity or the accumulation of residual impurities), the pattern is stationary. The interesting fact is the existence of a good correlation between the local values of α and λ. The simplifying assumption that the local value of α is rapidly adjusted to the local value of λ can be made. (This assumption is certainly valid provided that the local gradient of λ is smaller than some value.) Then the diagrams obtained by plotting the local value of α as a function of the local value of λ can be assimilated to the $\alpha(\lambda)$ diagrams of the homogeneous (perfectly periodic) system. The $\alpha(\lambda)$ diagram of crystal *b* obtained in this way is shown in Fig. 19. The scatter in the $\alpha(\lambda)$ data points is higher than the measurement uncertainty because the pattern was not perfectly stationary. It is, however, clear that α increases when λ increases. Roughly speaking, the relation between α and λ is a linear one.

The dependence of α on *V* has been studied in another crystal of the same type of orientation, which was submitted to two successive solidification runs at two slightly different

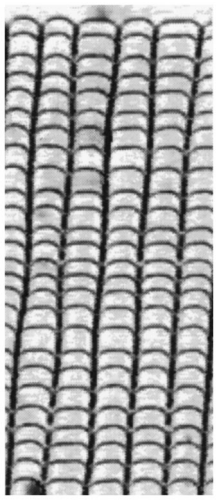

FIG. 20. Enlarged view of a detail of the ST diagram of Fig. 14 showing a patch of 2λ oscillations. Tiled-up images of the front taken at time intervals of 5 s are also shown. Total width of the image: 317 μm.

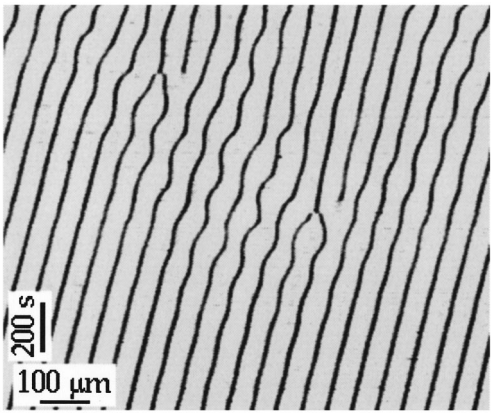

FIG. 21. ST diagram at $V=4.4\ \mu\mathrm{m\ s^{-1}}$ in a crystal of low-anisotropy nonaxial orientation.

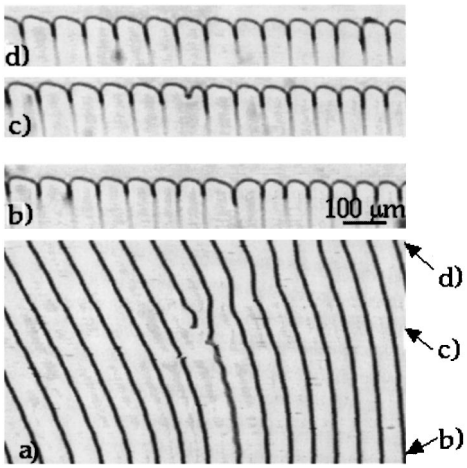

FIG. 22. Transient doublet observed in a nonaxially oriented crystal. $V=3.4\ \mu\mathrm{m\ s^{-1}}$. (a) ST diagram (recording duration $\approx$1500 s). (b), (c), and (d): snapshots at different times. Note that the doublet is destroyed by a tip splitting of one of its constituent cells, followed by the emission of a tilt wave. This wave is the only trace left behind by the whole process, showing that the doublet was not associated with a grain boundary.

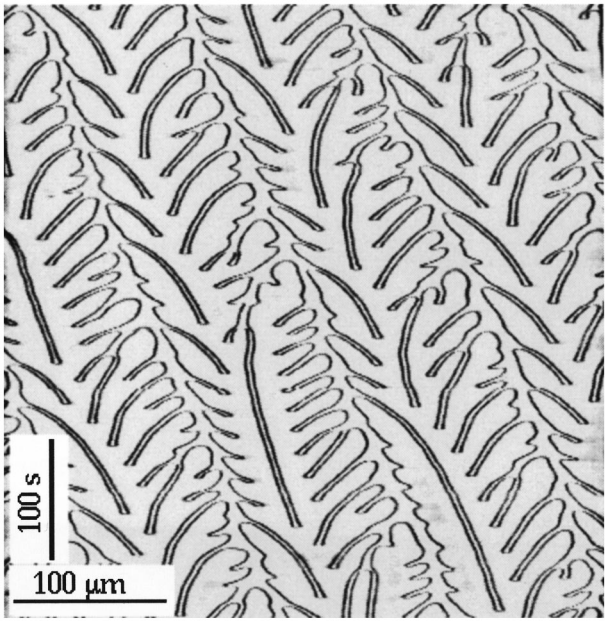

FIG. 23. ST diagram of a seaweed pattern in a nearly $\{111\}\langle uvw\rangle$-oriented crystal. $V=32\ \mu\mathrm{m\ s^{-1}}\approx 15V_c$ ($G=90\ \mathrm{K\ cm^{-1}}$). The slight tilt is due to some residual effective anisotropy [9].

velocities ($V_1=3.4\ \mu\mathrm{m\ s^{-1}}$, $V_2=3.7\ \mu\mathrm{m\ s^{-1}}$). The corresponding $\alpha(\lambda)$ diagrams are reported in Fig. 19 (circular symbols). It is found that α increases with increasing V and λ. Note that, contrary to what is observed in the dendritic velocity range, α increases much more rapidly with V than with λ.

D. The vanishing-anisotropy orientation (crystal *c*)

The most obvious feature of the disordered dynamics of the cellular pattern in crystal *c* (Fig. 14) is the occurrence of numerous cell-termination and tip-splitting events. A closer inspection, however, reveals that at least two other types of instabilities come into play, namely, the tilt and $2\lambda O$ instabilities. Figure 14 shows that each type of instability can trigger, and be triggered, by every other type of instability. No region in the stationary, symmetric state is seen, but large patches of the $2\lambda O$ pattern are observed. This suggests that the symmetric state, and *a fortiori* the $2\lambda O$ state, are not very far from being stable. An enlarged view of a $2\lambda O$ patch is shown in Fig. 20. The corresponding value of the time

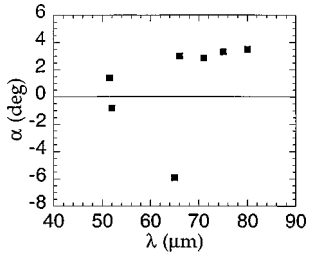

FIG. 24. Tilt angle as a function of spacing in crystal *d*. Data extracted from the ST diagram of Fig. 15. Positive α values correspond to leftward-tilted cells. Each data point results from the averaging of a number of measurements.

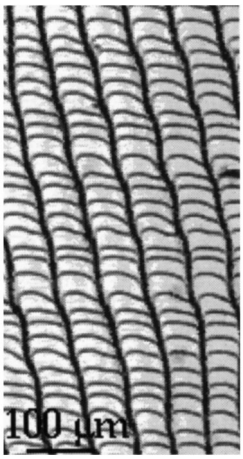

FIG. 25. Enlarged view of a detail of Fig. 15 showing the T-$1\lambda O$ mode. The time interval between the images of the front is of 5 s.

period of the oscillation is 350 ± 10 s. In that case, the 2λ oscillations were interrupted by their collision with a solitary tilt wave. In another case, shown in Fig. 21, the 2λ oscillations led to cell-termination and tip-splitting events occurring by pairs. The average spacing was thus globally preserved, but the phase matching of the oscillations was destroyed.

In a system without interfacial anisotropy, Kopczynski *et al.* [42] have found numerically several branches of stationary doublets (i.e., pairs of symmetry-broken cells) in the cellular velocity range. Cell doublets have also been found experimentally at $V\approx 2V_c$ in $\{001\}\langle 100\rangle$-oriented crystals of SCN-based alloys, which are known to have a very weak interfacial anisotropy [17,19]. In our system, we did not observe stationary doublets in the $\{111\}\langle uvw\rangle$ orientation, or in any other orientation. However, we occasionally encountered transitory, isolated doublets in regions of strong λ gradients (Fig. 22), indicating that the doublet branch also is not very far from being stable.

The ST diagram of crystal *c* is clearly different from the those of the seaweed patterns observed at higher velocity. For comparison, a ST diagram of the latter type is reproduced in Fig. 23. As explained in Part I, the main characteristic feature of such a diagram is the alternation of wide liquid grooves, delimiting stationary ''seaweed cells,'' and narrow liquid grooves, corresponding to transitory, but long-lived, doublons. No analog of this feature is seen in Fig. 14. A V jump to $4.1\ \mu\mathrm{m\ s^{-1}}$ ($\approx 1.9V_c$) applied at the end of the run did not provoke any noticeable change. Further observations in the range $2<V/V_c<5$ will be necessary to clarify

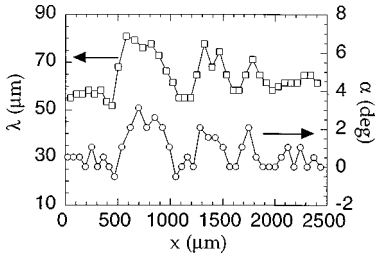

FIG. 26. Spacing- and tilt-angle-plots in crystal *e* at the time corresponding to the snapshot in Fig. 8(e).

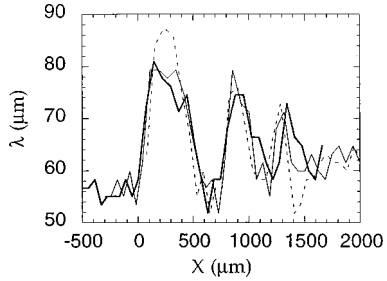

FIG. 27. Spacing as a function of $X=x-V_w t$, where V_w is the lateral-drift velocity of a tilt-domain wall (crystal *e*). Data extracted from Fig. 16 at times 0, 1325, and 2650 s.

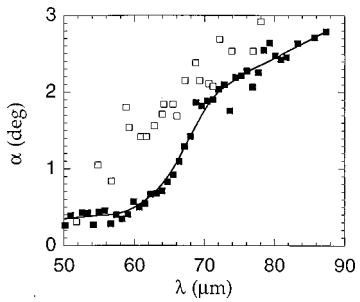

FIG. 28. Tilt angle as a function of spacing in crystal *e*. Data extracted from the ST diagram of Fig. 16. A time average was performed in order to reduce the dispersion due to the oscillations; the line is a guide for the eye. Open squares: values measured after a velocity jump from 3.4 to 3.75 μm s^{-1}.

the nature of the transition leading to the appearance of doublons.

E. The high-anisotropy degenerate orientation (crystal *d*)

The ST diagram observed in crystal *d* is shown in Fig. 15. A small downward *V* jump from 3.7 to 3.5 μm s^{-1} was applied at the end of the run. The existence of wide domains of oscillating tilted cells is obvious in this figure. The predominance of the domains of leftward-tilted cells is due to the in-plane misorientation of the crystal. Some domains of rightward tilted cells are also visible. The interdomain regions are too narrow to lend themselves to a detailed analysis (note, however, the transitory appearance of symmetric $2\lambda O$ cells in these regions).

In the λ plots of Fig. 10(d), the tilt domains appear as zones of large λ ($70\pm10\ \mu$m) and smooth λ profiles, whereas the interdomain regions are recognizable by their irregular λ distributions. The α plots extracted from the ST diagram are relatively inaccurate because of the oscillations. They nevertheless clearly bring to light the strong correlation existing between the local values of α and λ. The $\alpha(\lambda)$ diagram corresponding to Fig. 15 is shown in Fig. 24. The two directions of tilt appear as two separate branches. They are not mirror images of each other because of the in-plane misorientation of the crystal. The branch corresponding to the dominant leftward tilt exhibits a more or less linear dependence of α on λ, similar to the one found for the (single) branch in the nondegenerate orientations (see Fig. 19). The other branch is steeper and seems to go to zero at a relatively high value of λ. These features suggest a strongly imperfect tilt bifurcation, in which the continuous branch is the leftward-tilt branch, and the isolated branch the rightward-tilt branch.

The oscillations of the tilted cells are essentially of the T-$1\lambda O$ type (i.e., they are in phase over a given tilt domain). This is most clearly visible in Fig. 25, where an enlarged view of a portion of the ST diagram of Fig. 15 is shown. In this example, the time period of the oscillations is $t_{1\lambda}\approx150\pm30$ s, much longer than the diffusion time ($t_{1\lambda}/\delta\approx5$). A locking of the 1λ oscillation onto the drifting motion of the cells was previously conjectured for other systems [43]. It is therefore of interest to compare $t_{1\lambda}$ and the characteristic time $t_{\rm tilt}$ of the tilt, defined as $t_{\rm tilt}=\lambda/V_d$, where V_d is the lateral drift velocity of the cells. In the present case, $V_d\approx0.23\ \mu$m s^{-1}, $\lambda\approx75\ \mu$m, and $t_{\rm tilt}\approx330$ s$\approx2.2t_{1\lambda}$. In the case of crystal *e* (to be studied below), $t_{1\lambda}\approx230\pm20$ s, $V_d\approx0.17\ \mu$m s^{-1}, $\lambda=80\ \mu$m, and $t_{\rm tilt}\approx480$ s$\approx2.1t_{1\lambda}$. These two examples do not allow any definitive conclusion, but nevertheless suggest that $t_{\rm tilt}$ is equal to $2t_{1\lambda}$.

F. The low-anisotropy degenerate orientation (crystal *e*)

Figure 16 shows the ST diagram of crystal *e* pulled at $V_1=3.44\ \mu$m s^{-1}. The λ and α plots at the time corresponding to the snapshot in Fig. 8(e) are reproduced in Fig. 26. Clearly, the pattern consists of an alternation of domains of symmetric and (oscillating) tilted cells. In the symmetric domains, $\lambda=57\pm5\ \mu$m and α is small ($<0.5°$). In the tilt domains, $\lambda=75\pm5\ \mu$m and the average value of the tilt angle is $\bar{\alpha}\approx2.5°$. The domain walls, i.e., the regions separating two adjacent domains, are relatively narrow (note that the leading and trailing walls of tilt domains have a different profile; the former are about 1 cell wide, while the latter about 3 cells wide). In the tilt domains, the cells are drifting leftward, like the high-*V* dendrites, while the domain walls are drifting in the reverse direction (this is a geometrical consequence of the fact that no cell is eliminated or created on crossing the walls [44]). All the walls have practically the same drift velocity (the corresponding tilt angle is $\alpha_w\approx5.9°$), so that the width of the domains remains constant. The walls must be understood as kinks separating stationary states of the system. This is illustrated in Fig. 27, which shows several λ plots measured at time intervals of 10^3 s, plotted in the reference frame attached to the walls.

Patterns very similar to the above one were previously observed in other types of systems [44–46]. They are the result of the so-called mechanism of dynamical wavelength selection explained theoretically by Coullet *et al.* [46]. This mechanism appears in 1D modulated fronts presenting a homogeneous tilt bifurcation whose threshold spacing is a function of *V*. We can therefore conclude that such a bifurcation exists in our system for low-anisotropy degenerate crystal orientations. This conclusion is further supported by the following. The $\alpha(\lambda)$ diagram extracted from Fig. 16 is shown in Fig. 28. In spite of the relatively large scatter of the data, it is clearly a slightly imperfect direct-bifurcation diagram. A few additional data obtained after a velocity jump from 3.4 μm s^{-1} to 3.75 μm s^{-1}, which was applied at the end of the run, are also reported. They indicate that the bi-

furcation diagram shifts toward smaller values of λ when V increases, as it should.

V. CONCLUDING REMARKS

The theoretical conclusions that can be drawn from this study have been indicated above. The most important of them is that the stability of the cellular patterns in the fully nonlinear velocity range primarily depends on the level of interfacial anisotropy of the system. Hints in favor of this conclusion being of general validity for 2D solidification are given by the numerical results of Kopczynski *et al.* for a symmetrical system [32] and the comparison between our observations on CBr_4-C_2Cl_6 and those of several authors on SCN-based alloys [17–19]. Whether it is valid for 3D solidification also has not yet been clearly established, to our best knowledge. Careful experimental investigation of 3D solidification as a function of crystal orientation would be necessary to clarify this point.

ACKNOWLEDGMENTS

Thanks are also due to H. Savary and A.-M. Pougnet, of the Centre National d'Etudes des Télécommunications, France-Télécom, Bagneux, France, for providing us with zone-refined chemicals. The experiments are supported financially by the Centre National d'Etudes Spatiales, France.

[1] K. A. Jackson and J. D. Hunt, Acta Metall. **13**, 1212 (1965).
[2] W. W. Mullins and R. F. Sekerka, J. Appl. Phys. **35**, 444 (1964). See also D. J. Wollkind and L. A. Segel, Philos. Trans. R. Soc. London, Ser. A **268**, 351 (1970); and B. Caroli, C. Caroli, and B. Roulet, in *Solids Far from Equilibrium*, edited by C. Godréche (Cambridge University Press, Cambridge, England, 1992).
[3] See, for instance, G. P. Ivantsov [Dokl. Akad. Nauk SSSR **58**, 567 (1947)] for dendritic growth, J. W. Rutter and B. Chalmers [Can. J. Phys. **31**, 15 (1953)] for cellular growth, and C. Zener [Trans. AIME **167**, 550 (1946)] for lamellar eutectic growth.
[4] The kinetic coefficient is defined as $\beta = \Delta T_k / V$, where ΔT_k is the difference between the actual and the equilibrium value of the undercooling at the interface. When the solid-liquid interface is rough, ΔT_k is a linear function of V, and β is independent of V.
[5] Several valuable reviews on the theory of dendritic growth are available, for instance, those by J. S. Langer, in *Chance and Matter*, edited by J. Souletie, J. Vannimenus, and R. Stora (Elsevier, Amsterdam, 1987); D. A. Kessler, J. Koplik, and H. Levine, Adv. Phys. **37**, 255 (1988); H. Müller-Krumbhaar and W. Kurz, *Phase Transformation in Materials*, edited by P. Haasen (VCH-Verlag, Weinheim, 1991); Y. Pomeau and M. Ben Amar, in *Solids Far from Equilibrium*, edited by C. Godrèche (Cambridge University Press, Cambridge, England, 1992).
[6] E. A. Brener, H. Müller-Krumbhaar, and D. E. Temkin, Europhys. Lett. **17**, 535 (1992).
[7] T. Ihle and H. Müller-Krumbhaar, Phys. Rev. Lett. **70**, 3083 (1993); T. Ihle and H. Müller-Krumbhaar, Phys. Rev. E **49**, 2972 (1994).
[8] R. Kupferman, D. A. Kessler, and E. Ben-Jacob, Physica A **213**, 451 (1995).
[9] S. Akamatsu, G. Faivre, and T. Ihle, Phys. Rev. E **51**, 4751 (1995).
[10] R. Trivedi, V. Seetharaman, and M. A. Eshelman, Metall. Trans. **22A**, 585 (1991).
[11] S. R. Coriell and R. F. Sekerka, J. Cryst. Growth **34**, 157 (1976).
[12] M. Bennett, K. Tsiveriotis, and R. A. Brown, Phys. Rev. B **45**, 9562 (1992).
[13] W.-J. Rappel and H. Riecke, Phys. Rev. A **45**, 846 (1992).
[14] P. Coullet and G. Iooss, Phys. Rev. Lett. **64**, 866 (1990).
[15] J. T. Gleeson and P. Cladys, Phys. Rev. Lett. **66**, 236 (1991).
[16] S. de Cheveigné and C. Guthmann, J. Phys. I **2**, 193 (1992).
[17] H. Jamgotchian, R. Trivedi, and B. Billia, Phys. Rev. E **47**, 4313 (1993).
[18] M. Georgelin, Thèse de Doctorat, Université d'Aix-Marseille I (1997); M. Georgelin and A. Pocheau, Phys. Rev. E **57**, 3189 (1998).
[19] M. Georgelin and A. Pocheau, Phys. Rev. Lett. **79**, 2698 (1997).
[20] W. L. Kaukler and J. W. Rutter, in *In Situ Composites*, edited by F. D. Lemkey, H. E. Cline, and M. McLean (Elsevier, Amsterdam, 1982), p. 305.
[21] J. Mergy, G. Faivre, C. Guthmann, and R. Mellet, J. Cryst. Growth **134**, 353 (1993).
[22] T. Ihle and S. Akamatsu (unpublished). The found values are $\beta_0 \approx 5 \times 10^{-3}$ K s μm^{-1}, and $\varepsilon_k \approx 0.1$. Numerical results show that kinetic effects predominate over capillary effects for any reasonable value of the anisotropy coefficient of γ. This is probably due to the high value (≈ 20) of the ratio $D\beta_0 / \Delta T_0 d_0$ (see text for definitions).
[23] P. Kurowski, C. Guthmann, and S. de Cheveigné, Phys. Rev. A **42**, 7368 (1990).
[24] K. Brattkus and C. Misbah, Phys. Rev. Lett. **64**, 1925 (1990). The limited extent of the weakly nonlinear range is due to the fact that $d_0 / l_{\rm th} \ll 1$ (for a definition, see the text) in our system, as is usually the case in directional solidification.
[25] S.-K. Chan, H.-H. Reimer, and M. Kahlweit, J. Cryst. Growth **32**, 303 (1976).
[26] E. A. Brener and V. I. Mel'nikov, Adv. Phys. **40**, 53 (1991).
[27] J. C. LaCombe, M. B. Koss, V. E. Fradkov, and M. E. Glicksman, Phys. Rev. E **52**, 2778 (1995); U. Bisang and J. H. Bilgram, Phys. Rev. Lett. **75**, 3898 (1995).
[28] A. Classen, C. Misbah, H. Müller-Krumbhaar, and Y. Saito, Phys. Rev. A **43**, 6920 (1991).
[29] Y. Saito, C. Misbah, and H. Müller-Krumbhaar, Phys. Rev. Lett. **63**, 2377 (1989).
[30] T. Okada and Y. Saito, Phys. Rev. E **54**, 650 (1996).
[31] S. Akamatsu and T. Ihle, Phys. Rev. E **56**, 4479 (1997).
[32] P. Kopczynski, W. J. Rappel, and A. Karma, Phys. Rev. Lett. **77**, 3387 (1996).
[33] M. Ginibre, S. Akamatsu, and G. Faivre, Phys. Rev. E **56**, 780 (1997).
[34] S. Akamatsu and G. Faivre, J. Phys. I **6**, 503 (1996).

[35] Image processing was made with the NIH-Image software on a Power Macintosh computer. NIH Image is a public domain program developed at the U.S. National Institutes of Health and available from the Internet by anonymous FTP from zippy.nimh.nih.gov or on floppy disk from the National Technical Information Service, Springfield, Virginia, part number PB95-500195GEI.

[36] V. G. Smith, W. A. Tiller, and J. W. Rutter, Can. J. Phys. **33**, 723 (1955). See also J. A. Warren and J. S. Langer, Phys. Rev. A **47**, 2702 (1993); B. Caroli, C. Caroli, and L. Ramirez-Piscina, J. Cryst. Growth **132**, 377 (1993).

[37] The solidification dynamics of our system at V close to $V_c(V/V_c-1\approx 0.1)$ seems to be dominated by three-dimensional effects involving wetting forces at the glass plates, which may be sensitive to residual impurities (unpublished observations). These effects become unimportant as soon as the amplitude of the cells is large compared to the sample thickness.

[38] P. Kurowski, S. de Cheveigné, G. Faivre, and C. Guthmann, J. Phys. (France) **50**, 3007 (1989).

[39] W. Huang, X. Geng, and Y. Zhou, J. Cryst. Growth **134**, 105 (1993).

[40] W. Losert, B. Q. Shi, and H. Z. Cummins, Proc. Natl. Acad. Sci. USA **95**, 431 (1998); **95**, 439 (1998).

[41] B. Caroli, C. Caroli, G. Faivre, and J. Mergy, J. Cryst. Growth **118**, 135 (1992).

[42] P. Kopczynski, W-J. Rappel, and A. Karma, Phys. Rev. Lett. **79**, 2698 (1997).

[43] See, e.g., F. Giorgiutti and L. Limat, Physica D **103**, 590 (1997).

[44] G. Faivre and J. Mergy, Phys. Rev. A **45**, 7320 (1992); **46**, 963 (1992).

[45] A. J. Simon, J. Bechhoefer, and A. Libchaber, Phys. Rev. Lett. **61**, 2574 (1988). See also J. M. Flesselles, A. J. Simon, and A. J. Libchaber, Adv. Phys. **40**, 1 (1991).

[46] P. Coullet, R. E. Goldstein, and G. H. Gunaratne, Phys. Rev. Lett. **63**, 1954 (1989). See also S. Fauve, S. Douady, and O. Thual, J. Phys. II **1**, 311 (1991); Phys. Rev. Lett. **65**, 385 (1990); B. Caroli, C. Caroli, and S. Fauve, J. Phys. I **2**, 281 (1992).